Journal of
Nanoscience and Nanotechnology
Vol. 8, 1272–1278, 2008

Improved Luminescence Properties of Europium Complexes Encapsulated into Mesoporous SBA-15

Suwen Li[1,2], Hongwei Song[1,*], Wenlian Li[1], Shaozhe Lu[1], and Xinguang Ren[1]

[1] *Key Laboratory of Excited State Physics, Changchun Institute of Optics, Fine Mechanics and Physics, Chinese Academy of Sciences, 16 Eastern Nan-Hu Road, Changchun 130033, P. R. China*
[2] *Graduate school of Chinese academy of Sciences, Beijing 100039, P. R. China*

Two kinds of Eu^{3+} complexes—$Eu(TTA)_3(TPPO)_2$ (TTA: thenoyltrifluoroacetone, TPPO: triphenylphosphineoxide) and $Eu(BA)_3(TPPO)_2$ (BA: 1-benzoylacetone)—were fully encapsulated, uniformly distributed into the channels of unmodified and modified SBA-15, and structurally characterized. The luminescent properties of the encapsulated complexes were systematically studied in contrast to the pure complexes. The results indicate that the excitation bands assigned to the $\pi-\pi^*$ electron transition of the ligands for Eu^{3+} complexes encapsulated in SBA-15 were split into different components, and the $^5D_0$-$^7F_0$ transitions became partly allowed. The emission lines for the $^5D_0$-$^7F_2$ transitions became broader and the relative intensity for different crystal field components varied greatly in comparison to the pure complex. Most importantly, the photostability and thermostability of the emissions improved considerably.

Keywords: Europium Complexes, Mesoporous SBA-15, Photoluminescence, Photostability, Thermostability.

RESEARCH ARTICLE

1. INTRODUCTION

Rare earth (RE) complexes often show efficient luminescence due to the strong absorption of the ligands and the effective intramolecular energy transfer from the triplet state of ligands to central RE ions, which in turn undergoes the corresponding radiative emitting process (the so-called "antenna effect").[1] RE complexes are of considerable interest in the development of advanced luminescent materials and photoelectronic applications such as laser materials[2] or luminescent biological labels.[3,4] However, RE complexes have limited practical use because of their poor thermal stability and mechanical properties, although they have good phosphor characteristics.[5] Recently, because their photophysical properties can be modified by interaction of the host structure, the luminescence properties of RE complexes supported on a solid matrix have been extensively studied. For instance, the RE complexes were encapsulated in or adsorbed on host materials, including Langmuir-Blodgett films,[6] porous glasses,[7] sol–gel matrices,[8,9] oxide surfaces,[10] zeolites,[11,12] and silica matrices.[13] Among them, the mesoporous molecular sieves used as a support for RE complexes have attracted particular attention. In the past few years, Xu,[14,15] Zhang,[16] and Fernandes et al.[17] encapsulated different ternary Eu^{3+} complexes into channels of MCM-41 via wet impregnation and observed that encapsulation of the ternary Eu^{3+} complexes in MCM-41 gave efficient red emissions. Further, Xu et al. observed that in the encapsulated samples, Eu^{3+} complexes had better photostability under UV irradiation than the corresponding pure complexes. However, the improvement of photostability was too limited, and the thermostability of this kind of materials has not been studied.

To overcome the problem caused by the wet impregnation,[18] we adopted a combined method of pressure difference and wet impregnation to encapsulate two kinds of Eu^{3+} complexes—$Eu(TTA)_3(TPPO)_2$ (TTA: thenoyltrifluoroacetone, TPPO: triphenylphosphineoxide) and $Eu(BA)_3(TPPO)_2$ (BA: 1-benzoylacetone)—into the channels of SBA-15, which ensured that the RE complexes could be effectively filled into the channels of SBA-15. SBA-15 was adopted because it may provide a better support for Eu^{3+} complexes owing to its larger pore size and better stability in comparison with MCM-41.[19] In order to thoroughly understand the photoluminescence properties of this kind of materials, the spectral properties were systematically studied. It is interesting to observe that in SBA-15, the photostability and thermostability of both kinds of Eu^{3+} complexes were improved considerably.

*Author to whom correspondence should be addressed.

1533-4880/2008/8/1272/007 doi:10.1166/jnn.2008.350

2. EXPERIMENTAL DETAILS

Pure $Eu(TTA)_3(TPPO)_2$ and $Eu(BA)_3(TPPO)_2$ complexes (labeled **A** and **B**, respectively) were synthesized according to the literature.[20] The resulting complexes had the following molecular structures:

(A)

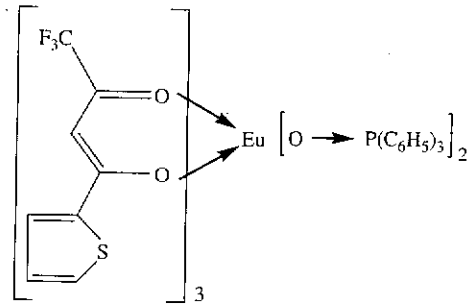

(B)

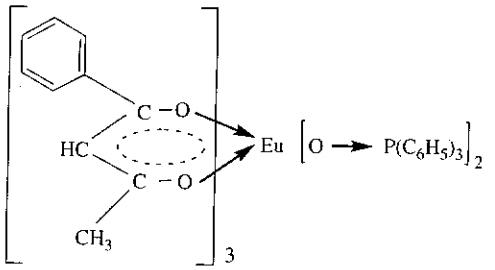

The SBA-15 was purchased from Jilin University. Some of the SBA-15 was used as received, and some was modified with 3-aminopropyltriethoxysilane (APTES) (Fluka), as described in the literature.[21] The precursor solution was prepared by dissolving appropriate amounts of the pure **A** or **B** complexes in chloroform solution. 100 mg of dried SBA-15 was decompressed in a 100 ml round-bottomed flask. When the pressure was isobaric, the precursor solution was slowly added to the round-bottomed flask. Then, the pressure was removed, and the solution was placed in air for 24 h. The mixture was filtered and washed with acetone until the color (red) of the filtered solution disappeared under the irradiation of a 355-nm laser light. Finally, the resultant products were dried for 2 h in vacuum, and labeled as samples $\mathbf{A}_1$ and $\mathbf{B}_1$. Pure **A** and **B** complexes were encapsulated in the modified SBA-15 (MSBA) (labeled as samples $\mathbf{A}_2$ and $\mathbf{B}_2$) using a similar method.

The morphologies of the samples were characterized by a JEOL JEM-2010 transmission electron microscope (TEM) with an accelerating voltage of 200 kV. The X-ray diffraction (XRD) patterns of the samples were examined by a Rigaku Dmax-B X-ray diffractometer. The Fourier transform infrared (FTIR) spectra were recorded at a Bio-Rad FTS-3000 (EXCALIBUR SERIES) spectrometer. The UV-vis absorption spectra were recorded with a UV-VIS-NIR scanning spectrophotometer (SHIMADZU). The excitation and emission spectra were recorded at room temperature using a Hitachi F-4500 spectrophotometer equipped with a continuous 150 W Xe-arc lamp. The continuous light separated from a 500 W xenon lamp was used as irradiation with a line width of 10 nm and a power density of 10–100 $\mu W/cm^2$. To measure the temperature dependence of the emission intensity, the samples were put into a liquid nitrogen cycling system, in which the temperature varied from 77 to 300 K. 325-nm light from a He-Cd laser was used for excitation. The spectra were recorded by a UV-Lab Raman Infinity with resolution of 2 cm^{-1}. In the measurements of fluorescence dynamics, a 355-nm light generated from the Nd^{3+}: YAG laser combined with a fourth-harmonic-generator was used as pumping, with a repetition frequency of 10 Hz and duration of 10 ns. A TEKTRONIX TDS-3052 oscilloscope with a two-channel color digital phosphor was used to record fluorescence decay curves.

3. RESULTS AND DISCUSSION

3.1. Morphology and Structure

Figure 1 shows the XRD patterns of SBA-15. The XRD patterns show three characteristic diffraction peaks, which are indexed to (100), (110), and (200) planes, being typical peaks of two-dimensional hexagonal (*p6mm*) SBA-15. The nitrogen adsorption and desorption isotherms display type IV isotherm curves with an H1 hysteresis loop at a relatively high pressure, indicating the presence of large pores with narrow pore size distribution. The textural data of the materials are summarized as follows: BET surface area = 832.0580 m^2/g; pore diameter = 6–7 nm; and pore volume = 1.26 cm^3/g.

Figure 2 shows TEM images of SBA-15, modified SBA-15, and samples $\mathbf{A}_1$ and $\mathbf{A}_2$. It can be seen that the average pore diameter of unmodified SBA-15 is 6–7 nm, while the diameter of the modified SBA-15 decreases to 4–5 nm. Figures 2(c) and (d) demonstrate that the pores are fully filled in samples $\mathbf{A}_1$ and $\mathbf{A}_2$. The TEM images for the samples $\mathbf{B}_1$ and $\mathbf{B}_2$ are similar to Figures 2(c) and (d).

Figure 3 shows the FTIR absorption spectra of various samples. It can be seen that the vibration modes in the unmodified SBA-15 are consistent with those of

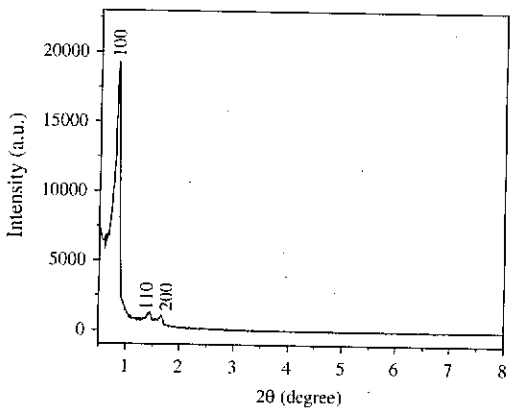

Fig. 1. XRD pattern of SBA-15.

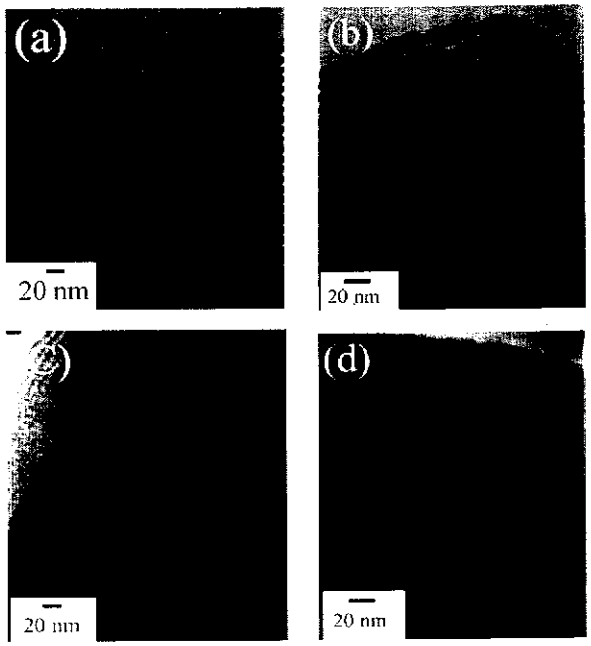

Fig. 2. TEM images of SBA-15 (a), modified SBA-15 (b), samples $\mathbf{A}_1$ (c), and $\mathbf{A}_2$ (d).

typical SBA-15 with *p6mm* phase. In comparison with the unmodified SBA-15, two additional peaks are observed in the modified SBA-15 at ~2934 cm^{-1} corresponding to the C—H stretching mode and at ~1564 cm^{-1} corresponding to the N—H bending mode in the primary ammine. In addition, a weaker peak appears at ~970 cm^{-1} in the unmodified SBA-15, which is assigned to Si—OH vibration generated by the presence of defect sites, which is a characteristic of mesoporous silica.[22] In the modified SBA-15, the intensity of the peak at 970 cm^{-1} decreases and changes into a shoulder at the same frequency. Accordingly, we suggest that some of $-CH_2NH_2$ groups were grafted onto the surface SBA-15 via reactions between silylating agents (APTES) and OH groups on the channel wall, as follows:

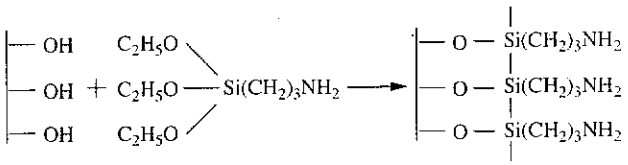

In Figure 3, a number of sharp vibration peaks appear in the range of 600–1660 cm^{-1} for the pure **A** complexes, while they do not appear in the samples $\mathbf{A}_1$ and $\mathbf{A}_2$. This suggests that the pure complexes were actually encapsulated in the pores of the host material but not physically absorbed outside. Similarly, the pure **B** complexes were considered to be encapsulated in the pores of the host material but not physically absorbed outside.

UV-vis absorption spectra of different samples are shown in Figure 4. For sample **A**, two absorption bands are observed around 268 and 340 nm which correspond to the π–π^* transitions of the ligands for the pure complexes. In contrast to the pure **A** complexes, the locations of the two bands in sample $\mathbf{A}_1$ are nearly the same, which indicates that the pure complexes were dispersed in the channels of unmodified SBA-15. In sample $\mathbf{A}_2$, both the two absorption bands become broader. In addition, the band at 268 nm blue-shifts to 254 nm, which is attributed to a strong H-bonding interaction between the F atomus of the **A** complexes and the $-NH_2$ groups of the modifying agent.[14] For sample **B**, the two absorption bands corresponding to the π–π^* transition of the ligands for the

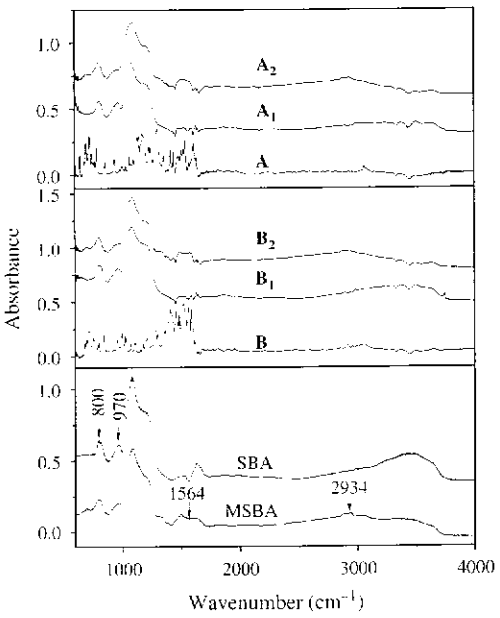

Fig. 3. FTIR spectra of the SBA-15, modified SBA-15, and samples **A**, $\mathbf{A}_1$, $\mathbf{A}_2$, **B**, $\mathbf{B}_1$, and $\mathbf{B}_2$.

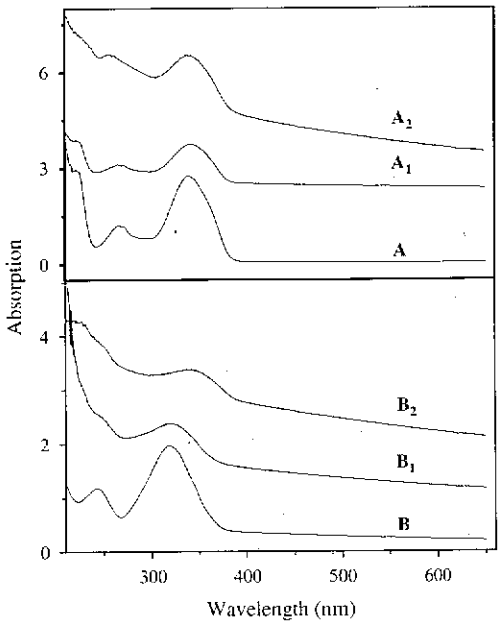

Fig. 4. UV-vis absorption spectra of the samples **A**, $\mathbf{A}_1$, $\mathbf{A}_2$, **B**, $\mathbf{B}_1$ and $\mathbf{B}_2$.

pure **B** complexes are located around 242 and 318 nm. In contrast to the pure **B** complexes, the locations of the two bands in sample $\mathbf{B}_1$ are nearly same. In sample $\mathbf{B}_2$, both absorption bands become broader, and the band at 318 nm red-shifts to 342 nm. The red-shift for the π–π^* transition of the ligands in the modified SBA-15 can be attributed to the inducement interaction between NH groups and the complexes, generating a nephelauxetic effect and decreasing the conjugation in the Eu^{3+} complexes.[23]

3.2. Excitation and Emission Spectra

It is well-known that in the RE complexes, energy is transferred from the triplet state of ligands to the center RE ion, which raises the $4f$ electron of the ions to excited energy levels. Radiative electronic transitions back to the ground state or to other lower states give off photons. Due to the shielding effect of electrons in the outer shells, inner $4f$ electronic transitions of the RE ions give rise to a narrow emission band that is insensitive to the chemical environments. The sensitization pathway in luminescent RE complexes generally consists of an initial strong absorption of ultraviolet energy that excites the ligand to the excited singlet (S_1) state, following by an energy migration via intersystem crossing from the S_1 state to a ligand triplet (T) state. The energy is then nonradiatively transferred from the lowest triplet state of the ligand to a resonance state of a coordinated lanthanide ion, which in turn undergoes a multiphoton relaxation and subsequent emission in the visible region.[24, 25]

The excitation spectra at room temperature and high-resolution emission spectra at 77 K for various samples are depicted in Figure 5(a). From the excitation spectra it can be seen that for the pure complex **A** or **B**, there exists a broad excitation band ranging from 200 to 480 nm, which is assigned to the π–π^* electron transition of the ligands. The $^7F_0$-$^5D_2$ inner shell excitation line can be also observed. For the encapsulated samples, the excitation bands are split into different components and disappear on the long wavelength side, which is attributed to the degenerated crystal field. For sample $\mathbf{A}_1$ or $\mathbf{A}_2$, there appears a main peak at ~344 nm and a shoulder at ~276 nm. For sample $\mathbf{B}_1$, three peaks appear at 239, 275, 335 nm, and for the sample $\mathbf{B}_2$, two peaks appear at 253 and 312 nm. It should be noted that in all the encapsulated samples, the $^7F_0$-$^5D_2$ inner-shell excitation line disappears. This suggests that in the composites, the f–f inner-shell transitions are quenched through the nonradiative energy transfer from the higher excited states to some uncertain defect levels, substituting for the nonradiative relaxation from higher excited states to $^5D_0$.

The high-resolution spectra also show some distinctive differences between the pure complexes and the encapsulated samples. In both the pure complexes, **A** and **B**, only the $^5D_0$-$^7F_1$ and $^5D_0$-$^7F_2$ lines appear and the $^5D_0$-$^7F_0$ emissions disappear completely. In the encapsulated complexes,

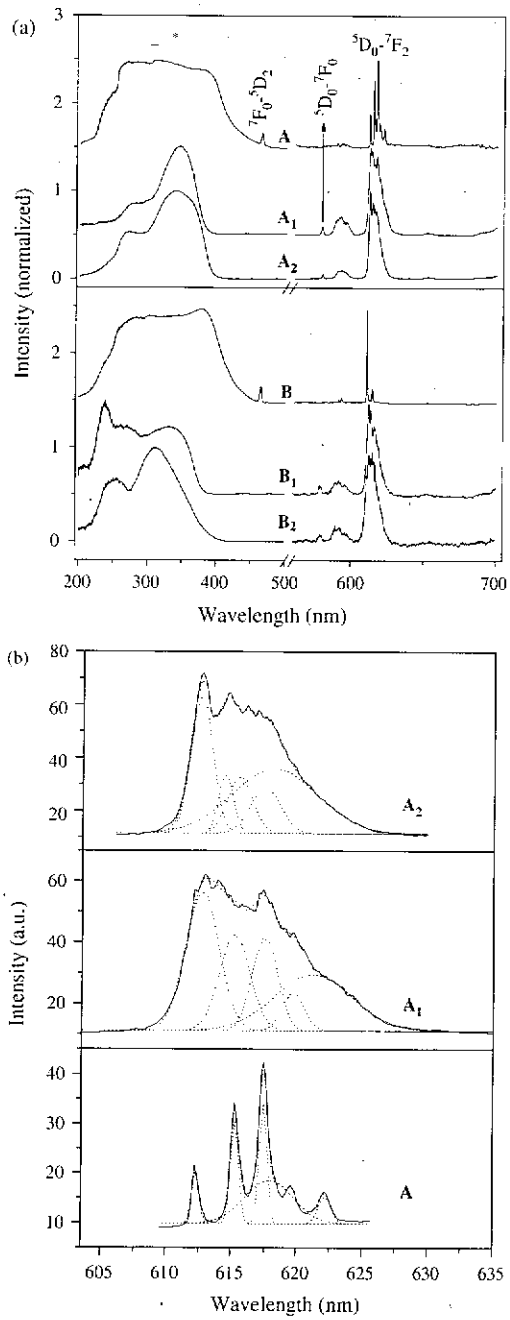

Fig. 5. (a) Excitation spectra of the samples **A**, $\mathbf{A}_1$, $\mathbf{A}_2$, **B**, $\mathbf{B}_1$ and $\mathbf{B}_2$ at room temperature and emission spectra of $^5D_0$-^7F_J ($J = 0$–4) transitions at 77 K ($\lambda_{ex} = 355$ nm), (b) fitting excitation spectrum of the samples **A**, $\mathbf{A}_1$, and $\mathbf{A}_2$ by a five-fold Gaussian function.

the $^5D_0$-$^7F_0$ emissions can be identified. This indicates that the electronic-dipole $^5D_0$-$^7F_0$ emissions become partly allowed due to the degenerated crystal field, while it is completely forbidden in the pure complexes. In complex **A**, five crystal-field splitting lines of $^5D_0$-$^7F_2$ can be observed at 612, 615, 617, 620 and 622 nm. The line at 617 nm is strongest. In the encapsulated complexes $\mathbf{A}_1$ and $\mathbf{A}_2$, due to more disordered local environments surrounding Eu^{3+} caused by the influence of SBA-15, the

sublines of $^5D_0$-$^7F_2$ are broadened inhomogeneously and overlapped with each other, forming a broad line with an intensity maximum at 612 nm. In Figure 5(b), the $^5D_0$-$^7F_2$ transitions for the samples $\mathbf{A_1}$, $\mathbf{A_2}$, and **A** are enlarged and dissolved into different components by a five-fold Gaussian function. It can be seen that besides the spectral broadening and shift, the relative intensity for different Stark components in the encapsulated complexes also varies greatly in comparison to the pure complex, indicating that in the encapsulated complexes the electronic transition rates from $^5D_0$ to different sublevels of $^7F_2$ change greatly. In Figure 5(a), two $^5D_0$-$^7F_2$ sublines can be observed in the pure **B** complexes, at 611 and 615 nm. The sublines of $^5D_0$-$^7F_2$ in the encapsulated complexes are similarly broadened to one line.

3.3. Photoluminescence Stability

It is well-known that the instability of RE complexes under UV irradiation is one of the problems for practical application. In the present work, the dependence of emission intensity on irradiation time was studied for different samples. As shown in Figure 6, the emission intensity of the $^5D_0$-$^7F_2$ transition for pure **A** and **B** complexes decreases obviously with increasing exposure time, while it is clear that in the samples $\mathbf{A_1}$, $\mathbf{A_2}$, $\mathbf{B_1}$, and $\mathbf{B_2}$ the photoluminescence is much more stable than in the corresponding pure complexes. Here, the intensity in samples $\mathbf{A_1}$ and $\mathbf{B_1}$ is nearly constant, and the intensity in samples $\mathbf{A_2}$ and $\mathbf{B_2}$ initially increases and subsequently remain constant.

The unmodified and modified SBA-15 both provide a rigid environment for the pure complexes to reduce the energy consumption by the vibration of ligands and collision of intermolecular of complexes, and SBA-15 protects the pure complexes from decomposing under UV irradiation. The intensity enhancement with exposure time in samples $\mathbf{A_2}$ and $\mathbf{B_2}$ can be attributed to optical modification of the surface defects. In the preparation, a large number of surface defects are present in the inner surface of the pores, which generally act as nonradiative relaxation channels. Under exposure to UV light, the defects are gradually modified, causing the increase in photoluminescence. Xu et al. also observed improved photostability in the Eu complexes encapsulated in the porous MCM-41,[14,15] however, the degree of the improvement was not as large as the present results because in the present samples, the RE complexes are better distributed into the pores.

3.4. Temperature-Dependence of Emission Intensity

Figure 7 shows that the dependence of emission intensity on temperature under 325-nm excitation in various samples. It can be seen that the emission intensity of $^5D_0$-^7F_J for the Eu^{3+} ion in samples **A**, $\mathbf{A_1}$, **B**, $\mathbf{B_1}$, and $\mathbf{B_2}$ decreases uniformly with the increasing temperature in the studied range. In comparison with the pure **A** and **B** complexes, the emission intensity of $^5D_0$-^7F_J in samples $\mathbf{A_1}$, $\mathbf{B_1}$, and $\mathbf{B_2}$ changes more slowly. In contrast, the emission intensity of $^5D_0$-^7F_J for the Eu^{3+} ion in sample $\mathbf{A_2}$ initially increases with the increasing temperature, reaches to a maximum, and then it decreases as the temperature increases continuously. This complicated variation of florescence intensity is explained as follows. The emission intensity of the $^5D_0$-$^7F_2$ transitions depends on the thermal activation, phonon-assisted absorption, and the temperature-quenching

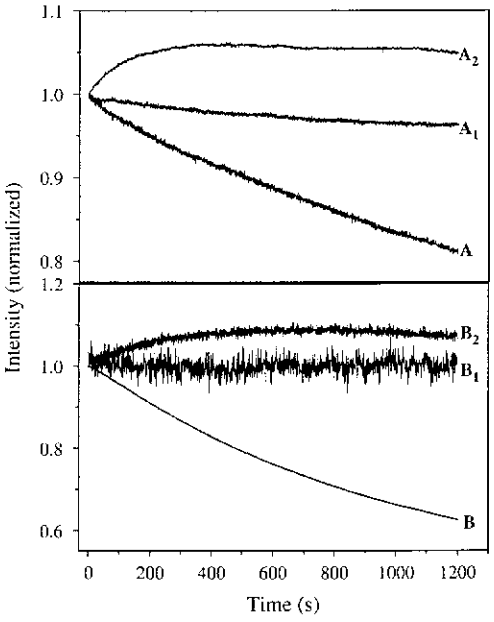

Fig. 6. Dependence of emission intensity at 611 nm on irradiation time for various UV lights, $\lambda_{ex} = 340$ nm for the samples **A**, $\mathbf{A_1}$, and $\mathbf{A_2}$, $\lambda_{ex} = 312$ nm for the samples **B**, $\mathbf{B_1}$, and $\mathbf{B_2}$.

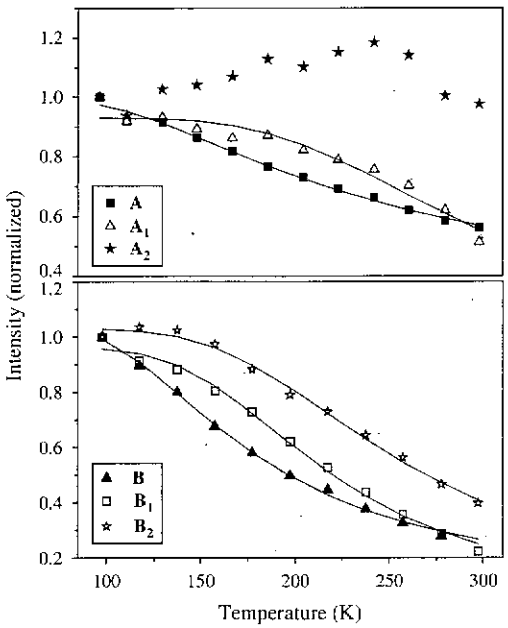

Fig. 7. Dependence of $^5D_0$-$^7F_2$ emission intensity on temperature in the samples **A**, $\mathbf{A_1}$, $\mathbf{A_2}$, **B**, $\mathbf{B_1}$, and $\mathbf{B_2}$ ($\lambda_{ex} = 325$ nm).

effect. When the temperature is high enough, phonon-assisted absorption occurs, and the efficiency of intramolecular energy migration from organic ligands to the central Eu^{3+} ion increases. These processes may cause the emission intensity of the Eu^{3+} ion to increase as the temperature increases. Actually, the temperature-quenching effect becomes strong as the temperature is elevated, which tends to cause the emission intensity of the Eu^{3+} ion to decrease. The temperature-quenching channels include the nonradiative transitions from $^5D_0$ to each ^7F_J level and the energy transfer from one excited Eu^{3+} ion to the other Eu^{3+} ion or to the other centers nearby. In the other samples, the thermal quenching contributes dominantly to the temperature dependence of the fluorescence intensity.

In Figure 7, the intensity as a function of temperature for samples **A**, $\mathbf{A_1}$, **B**, $\mathbf{B_1}$, and $\mathbf{B_2}$ can be fitted by the well-known thermal activation function:[26]

$$I(T) = \frac{I_0}{1 + \alpha e^{-E_A/K_B T}} \quad (1)$$

where I_0 is the emission intensity at 0 K, α is the proportional coefficient, E_A is the thermal activation energy, K_B is Boltzimann's constant, and T is the absolute temperature. The values of α and E_A obtained by fitting are listed in Table I. The improved value of E_A in the encapsulated complexes suggests that the photoluminescence is more stable than that in the corresponding pure complexes.

3.5. Fluorescence Dynamics

The fluorescence decay curves for the $^5D_0$-$^7F_2$ transitions of Eu^{3+} ions in different samples under 355-nm excitation were measured at room temperature, as shown in Figure 8. It can be seen that the $^5D_0$-$^7F_2$ transitions all decay exponentially for different samples. The exponential lifetimes in all the samples were obtained by the dynamics, as listed in Table I. It is apparent that the lifetimes in samples $\mathbf{A_1}$ and $\mathbf{B_1}$ are shorter than in the pure **A** and **B** complexes, while the lifetimes in samples $\mathbf{A_2}$ and $\mathbf{B_2}$ are longer. This can be mainly attributed to variation of refractive index surrounding the Eu^{3+} ions.

In fact, the lifetime of $^5D_0$, τ is dominated by the total radiative transition rate of $^5D_0$-$\Sigma^7F_J W_r$, and the nonradiative decay rate W_{nr}, which can be written as[27]

$$\tau = \frac{1}{W_r + W_{nr}} \quad (2)$$

Table I. The fitting parameters α, E_A according to Eq. (1) in the text, lifetime of the $^5D_0$-$^7F_2$ transition (at 613 nm) of Eu^{3+} ions.

Samples	α	E_A (meV)	Lifetime (μs)
A	3.0	35.6	446.2
$\mathbf{A_1}$	25.7	93.3	332.2
$\mathbf{A_2}$	—	—	702.2
B	19.8	48.9	547.2
$\mathbf{B_1}$	69.2	81.9	306.0
$\mathbf{B_2}$	48.2	88.7	762.1

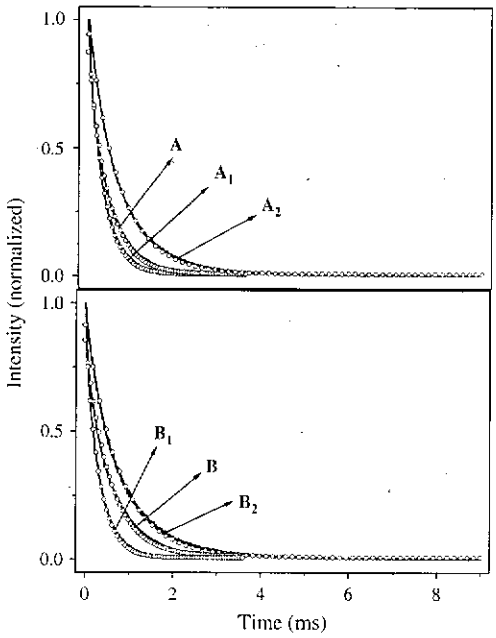

Fig. 8. Fluorescent decay curves of the $^5D_0$-$^7F_2$ transitions at 613 nm in various samples (λ_{ex} = 355 nm). The solid lines are experimental data, and the circle are fitting functions.

where W_{nr} includes the nonradiative relaxation rate from $^5D_0$ to lower ^7F_J levels and nonradiative energy transfer rate to the other defect centers. In the unmodified samples $\mathbf{A_1}$ and $\mathbf{B_1}$, the SBA-15 may adsorb some water on the surface (Fig. 3), which may act as a luminescence quencher resulting in improved nonradiative relaxation.[27] The improved nonradiative relaxation led to the decrease of fluorescence decay time. In the modified samples $\mathbf{A_2}$ and $\mathbf{B_2}$, the increase of fluorescence lifetime can be attributed to the influence of the surrounding media (MSBA). The radiative lifetime can be written as[28]

$$\tau_R \approx \frac{1}{f(\mathrm{ED})} \frac{\lambda_0^2}{\left[\frac{1}{3}(n^2+2)\right]^2 n} \quad (3)$$

where f(ED) is the oscillator strength for the electronic dipole transition, λ_0 is the wavelength in vacuum and n is the refractive index of the material. Meltzer et al. observed that the radiative fluorescence lifetime of Y_2O_3:Eu^{3+} nanocrystals is dependent on not only the refractive index, but also the surrounding medium. They deduced that in nanoparticles, n in Eq. (3) should be substituted by the effective refractive index

$$n_{\mathrm{eff}} = xn + (1-x)n_{\mathrm{med}} \quad (4)$$

where x is the filling factor showing what fraction of the space is occupied by the nanoparticles, and n_{med} is the refractive index of the surrounding media.[28] In the present case, the complexes are surrounded by SBA-15 mesoporous molecule sieves. The refractive index values are 1.15 for SBA-15,[29] 1.56 for TTA in sample **A**, 1.72 for BA in sample **B**, and 1.72 for TPPO in both samples.

The decreased refractive index of the surrounding media will lead n_{eff} to be smaller than the refractive index of the complex n which would induce the increase of radiative lifetime. In the unmodified samples, the existence of the surrounding media SBA-15 should also cause the radiative transition rate of Eu^{3+} in the complex to decrease. However, the decrease of the radiative transition rate should be smaller than the increase of the nonradiative transition rate. Therefore, the total electronic transition rate increases, leading to the decrease of fluorescence lifetime. On the other hand, in the modified samples, the adsorbed water should also influence the nonradiative transition rate, but because the water content is not high enough, the influence of adsorbed water on nonradiative transition rate can be neglected in comparison to the variation of the radiative transition rate.

4. CONCLUSIONS

We encapsulated and characterized the RE complexes $Eu(TTA)_3(TPPO)_2$ and $Eu(BA)_3(TPPO)_2$ in unmodified and modified SBA-15, which provided a rigid environment for the RE complexes. Their photoluminescence properties were systemically studied in contrast to the pure complexes. The results demonstrated that in the unmodified and modified SBA-15, the excitation bands corresponding to the π–π^* electron transition of the ligands were split into different sharp components due to decreased symmetry, and the components of long wavelength nearly disappeared for both $Eu(TTA)_3(TPPO)_2$ and $Eu(BA)_3(TPPO)_2$ complexes. Sharp $^5D_0$-^7F_J lines ($J = 0$–2) were observed in the encapsulated samples, and the $^5D_0$-$^7F_2$ electronic dipole lines were dominant. It is interesting to observe that in the encapsulated complexes, the electronic dipole $^5D_0$-$^7F_0$ emission becomes partly allowed, while it is completely forbidden in the pure complexes. The lifetime of Eu^{3+} in samples $\mathbf{A_1}$ and $\mathbf{B_1}$ becomes shorter than that in the pure **A** and **B** complexes, respectively, while that in the sample $\mathbf{A_2}$ and $\mathbf{B_2}$ becomes longer. It can be attributed to the influence of adsorbing water on the surface and the effect of the refractive index of the SBA-15 surrounding the Eu^{3+} complexes.

For samples encapsulated into the unmodified and modified SBA-15, the photostability of the Eu^{3+} complexes is improved considerably in comparison to the pure complexes. In the modified samples, it is interesting to observe that the emission intensity increases with increasing irradiation time, which is attributed to the modification of surface defects under exposure to ultraviolet lights. The thermal stability for the samples encapsulated in SBA-15 is also improved considerably. Overall, the photoluminescence properties of Eu^{3+} complexes encapsulated in SBA-15 are improved in comparison to the pure complexes, which is essential for future applications of RE complexes in molecular optical and electrical devices.

Acknowledgment: The author thanks the financial support by National Natural Science Foundation of China (Grants 10374086 and 10504030) and Talent Youth Foundation of JiLin Province (Grants 20040105).

References and Notes

1. S. Sato and M. Wada, *Bull. Chem. Soc. Jpn.* 43, 1955 (**1970**).
2. H. Yokoyama, *Science* 256, 66 (**1992**).
3. F. S. Richardson, *Chem. Rev.* 82, 541 (**1982**).
4. G. E. Buonocore, H. Li, and B. Marciniaak, *Coord. Chem. Rev.* 99, 55 (**1990**).
5. F. A. Hart and F. P. Laming, *J. Inorg. Nucl. Chem.* 27, 1825 (**1965**).
6. O. A. Serra, I. L. V. Rosa, C. L. Medeiros, M. Elizabete, and D. Zaniquelli, *J. Lumin.* 60–61, 112 (**1994**).
7. D. Avnir, D. Levy, and R. Reisfeld, *J. Phys. Chem.* 88, 5956 (**1984**).
8. L. R. Matthews and E. T. Knobbe, *Chem. Mater.* 5, 1697 (**1993**).
9. G. Qian, M. Wang, M. Wang, X. Fan, and Z. Hong, *J. Mater. Sci. Lett.* 16, 322 (**1997**).
10. M. F. Hazenkamp, G. Blasse, and N. Sabbatini, *J. Phys. Chem.* 95, 783 (**1991**).
11. I. L. V. Rosa, O. A. Serra, and E. J. Nassar, *J. Lumin.* 72–74, 532 (**1997**).
12. M. Alvaro, V. Forne's, S. Garcia, H. Garcia, and J. C. Scaiano, *J. Phys. Chem. B* 102, 8744 (**1998**).
13. R. J. Zhang and K. Z. Yang, *Langmuir* 13, 7141 (**1997**).
14. Q. Xu, L. Li, B. Li, and R. Xu, *Micropor. and Mesopor. Mater.* 38, 351 (**2000**).
15. Q. Xu, L. Li, X. S. Liu, and R. Xu, *Chem. Mater.* 14, 549 (**2002**).
16. M. S. Zhang, W. Yin, Q. Su, and H. J. Zhang, *Mater. Lett.* 57, 940 (**2002**).
17. A. Fernandes, J. Dexpert-Ghys, A. Gleizes, A. Galarneau, and D. Brunel, *Micropor. and Mesopor. Mater.* 83, 35 (**2005**).
18. R. Hernandez, A. Franville, P. Minoofar, B. Dunn, and J. I. Zink, *J. Am. Chem. Soc.* 123, 1248 (**2001**).
19. D. Zhao, Q. Huo, J. Feng, B. F. Chmelka, and G. D. Stucky, *J. Am. Chem. Soc.* 120, 6024 (**1998**).
20. B. Yan, H. J. Zhang, S. B. Wang, and J. Z. Ni, *Mater. Chem. Phys.* 51, 92 (**1997**).
21. T. S. Zemanian, G. E. Fryxell, J. Liu, S. Mattigod, J. A. Franz, and Z. Nie, *Langmuir* 17, 8172 (**2001**).
22. Q. L. Cheng, V. Pavlinek, A. Lengalova, C. Z. Li, Y. He, and P. Saha, *Micropor. and Mesopor. Mater.* 93, 263 (**2006**).
23. M. Latva, H. Takalo, V. M. Mukkala, C. Matachescu, and J. C. Rodriguez-Ubis, *J. Lumin.* 75, 149 (**1997**).
24. M. Tanaka, G. Yamagughi, J. Shiokawam, and C. Yamanaka, *Bull. Chem. Soc. Jpn.* 43, 549 (**1970**).
25. A. V. Haynes and H. G. Drickamer, *Chem. Phys.* 76, 114 (**1982**).
26. B. S. Li, Y. C. Liu, Z. Z. Zhi, D. Z. Shen, Y. M. Lu, J. Y. Zhang, and X. W. Fan, *J. Cryst. Growth* 240, 479 (**2002**).
27. S. W. Li, H. Song, W. Li, X. Ren, S. Lu, G. Pan, L. Fan, H. Yu, H. Zhang, R. Qin, Q. Dai, and T. Wang, *J. Phys. Chem. B* 110, 23164 (**2006**).
28. R. S. Meltzer, S. P. Feofilov, B. Tissue, and H. B. Yuan, *Phys. Rev. B* 60, 14012 (**1999**).
29. M. H. Bartl, S. W. Boettcher, K. L. Frindell, and G. D. Stucky, *Acc. Chem. Res.* 38, 263 (**2005**).

Received: 8 December 2006. Accepted: 2 May 2007.